

## Article

# Largely Enhanced Thermoelectric Power Factor of Flexible $\text{Cu}_{2-x}\text{S}$ Film by Doping Mn

Xinru Zuo, Xiaowen Han, Yiming Lu, Ying Liu, Zixing Wang, Jiajia Li and Kefeng Cai \* 

Key Laboratory of Advanced Civil Engineering Materials of Ministry of Education, Shanghai Key Laboratory of Development and Application for Metal-Functional Materials, School of Materials Science & Engineering, Tongji University, Shanghai 201804, China; 2132856@tongji.edu.cn (X.Z.); 18616350526@163.com (X.H.); 1651650@tongji.edu.cn (Y.L.); liuying\_polymer@163.com (Y.L.); wzxing2023@163.com (Z.W.); sduljj2018@163.com (J.L.)

\* Correspondence: kfcai@tongji.edu.cn

**Abstract:** Copper-sulfide-based materials have attracted noteworthy attention as thermoelectric materials due to rich elemental reserves, non-toxicity, low thermal conductivity, and adjustable electrical properties. However, research on the flexible thermoelectrics of copper sulfide has not yet been reported. In this work, we developed a facile method to prepare flexible Mn-doped  $\text{Cu}_{2-x}\text{S}$  films on nylon membranes. First, nano to submicron powders with nominal compositions of  $\text{Cu}_{2-x}\text{Mn}_y\text{S}$  ( $y = 0, 0.01, 0.03, 0.05, 0.07$ ) were synthesized by a hydrothermal method. Then, the powders were vacuum-filtrated on nylon membranes and finally hot-pressed. Phase composition and microstructure analysis revealed that the films contained both  $\text{Cu}_2\text{S}$  and  $\text{Cu}_{1.96}\text{S}$ , and the size of the grains was  $\sim 20\text{--}300$  nm. By Mn doping, there was an increase in carrier concentration and mobility, and ultimately, the electrical properties of  $\text{Cu}_{2-x}\text{S}$  were improved. Eventually, the  $\text{Cu}_{2-x}\text{Mn}_{0.05}\text{S}$  film showed a maximum power factor of  $113.3 \mu\text{W m}^{-1} \text{K}^{-2}$  and good flexibility at room temperature. Moreover, an assembled four-leg flexible thermoelectric generator produced a maximum power of 249.48 nW (corresponding power density  $\sim 1.23 \text{ W m}^{-2}$ ) at a temperature difference of 30.1 K, and had good potential for powering low-power-consumption wearable electronics.

**Keywords:**  $\text{Cu}_2\text{S}$ ; thermoelectric; hydrothermal synthesis; doping; flexible film



**Citation:** Zuo, X.; Han, X.; Lu, Y.; Liu, Y.; Wang, Z.; Li, J.; Cai, K. Largely Enhanced Thermoelectric Power Factor of Flexible  $\text{Cu}_{2-x}\text{S}$  Film by Doping Mn. *Materials* **2023**, *16*, 7159. <https://doi.org/10.3390/ma16227159>

Academic Editor: Cristiano Albonetti

Received: 23 October 2023

Revised: 7 November 2023

Accepted: 11 November 2023

Published: 14 November 2023



**Copyright:** © 2023 by the authors. Licensee MDPI, Basel, Switzerland. This article is an open access article distributed under the terms and conditions of the Creative Commons Attribution (CC BY) license (<https://creativecommons.org/licenses/by/4.0/>).

## 1. Introduction

Thermoelectric (TE) materials can directly convert heat into electricity and vice versa. This has attracted great attention for power generation and cooling [1]. With the growing demand for electrical appliances, there is an urge to produce renewable sources using flexible, eco-friendly, and economical materials. Flexible TE films (f-TEFs), which can fulfill this need, can generate electricity by utilizing the temperature difference ( $\Delta T$ ) between the human body and the environment [2]. The TE performance of a material is determined by the dimensionless figure of merit  $ZT$ , defined as  $ZT = \alpha^2 \sigma T / \kappa$ , where  $\alpha$  is the Seebeck coefficient,  $\sigma$  is the electrical conductivity,  $\kappa$  is the thermal conductivity,  $T$  is the absolute temperature, and  $\alpha^2 \sigma$  is called power factor (PF) that is related to electrical properties [3].

In recent years, substantial efforts have been mainly devoted to free-standing films [4–6] and films on flexible substrates [7–12]. For free-standing films, conductive polymers and their based composites have been widely studied due to their excellent flexibility and low thermal conductivity [13,14]. However, their  $ZT$  values still cannot be compared to those of inorganic TE materials. Inorganic films on flexible substrates can combine the flexibility of the substrate (such as polyimide, nylon, or paper) with the high  $ZT$  of inorganic TE materials, effectively balancing flexibility and TE performance [15]. For instance, a flexible p-type  $\text{Bi}_{0.4}\text{Sb}_{1.6}\text{Te}_3/\text{Te}$  composite film prepared on a Kapton surface by screen printing combined with pressure-less sintering (450 °C, 45 min) achieved a reasonably high PF value of  $\sim 3000 \mu\text{W m}^{-1} \text{K}^{-2}$  ( $ZT \sim 1$ ) at 300 K [9]. It showed a 3% increase in resistance after

1000 times bending around a 10 mm-radius rod. In 2019, our group developed a facile method to fabricate flexible  $\text{Ag}_2\text{Se}$  films on nylon membranes [7]: Se nanowires (NWs) were synthesized by a wet chemical method and used as templates to prepare  $\text{Ag}_2\text{Se}$  NWs, and  $\text{Ag}_2\text{Se}$  film was formed on porous nylon membranes by vacuum filtration and then hot-pressing (HP). The  $\text{Ag}_2\text{Se}$  films exhibited excellent flexibility and a PF of  $\sim 987 \mu\text{W m}^{-1} \text{K}^{-2}$  ( $ZT \sim 0.5$ ) at 300 K. Since then, we have worked to improve the PF [16–18]. For example, polypyrrole (PPy) was in situ polymerized to fabricate  $\text{Ag}_2\text{Se}/\text{Se}/\text{PPy}$  composite films on nylon membranes [17], and a PF of  $\sim 2240 \mu\text{W m}^{-1} \text{K}^{-2}$  at 300 K was achieved. Recently, Lei et al. [19] prepared  $\text{Ag}_2\text{Se}$  films by immersing Ag films sputtered on polyimide substrates into Se/ $\text{Na}_2\text{S}$  solution for selenization, and the PF at room temperature (RT) was  $\sim 2590 \pm 414 \mu\text{W m}^{-1} \text{K}^{-2}$ . Despite the excellent TE properties of  $\text{Bi}_2\text{Te}_3$  and  $\text{Ag}_2\text{Se}$  at RT, the elements Te and Se are not abundant and are toxic. So, for practical TE applications, it was necessary to search for low-cost inorganic materials without toxic elements.

Copper sulfide ( $\text{Cu}_{2-x}\text{S}$ ,  $0 \leq x \leq 0.25$ ), a typical liquid-like semiconductor [20], which has low lattice thermal conductivity [21], has been considered to be the candidate material to decouple electrical and thermal properties. Meanwhile, the elements Cu and S are abundant, cheap, and nontoxic; thus,  $\text{Cu}_{2-x}\text{S}$  is an economical and environmentally friendly TE material [22,23]. It forms a series of compounds ranging from copper-rich to copper-deficient, such as  $\text{Cu}_2\text{S}$ ,  $\text{Cu}_{1.96}\text{S}$ ,  $\text{Cu}_{1.92}\text{S}$ , and  $\text{Cu}_{1.8}\text{S}$ , whose crystal structures and TE performances vary with copper content. Typically,  $\text{Cu}_2\text{S}$  possesses a comparatively high  $\alpha$  of  $\sim 300 \mu\text{V K}^{-1}$  and poor  $\sigma$  ( $\leq 10 \text{ S cm}^{-1}$ ) at RT [24]. The crystal structure of  $\text{Cu}_2\text{S}$  undergoes complex change with increasing temperature: it is in a monoclinic-chalcocite phase at RT, which transforms into a hexagonal phase above 370 K and then into a cubic phase near 709 K [9,25]. The current research on copper-sulfide bulks mainly focuses on the medium and high-temperature regions. For example, Tang et al. [26] introduced a 3D graphene heterointerface into the  $\text{Cu}_{2-x}\text{S}$  matrix by mechanical alloying and spark plasma sintering (SPS) and obtained a high PF of  $1197 \mu\text{W m}^{-1} \text{K}^{-2}$  ( $ZT \sim 1.56$ ) at 873 K. And  $\text{Cu}_2\text{S}$  bulk incorporated Ag nanoparticles prepared by a hydrothermal method realized a high PF of  $1698 \mu\text{W m}^{-1} \text{K}^{-2}$  ( $ZT \sim 1.4$ ) at 773 K [27]. Recently, Li et al. [28] synthesized  $\text{Cu}_2\text{S}-\text{Cu}_{1.96}\text{S}$  phase junctions by retaining surface 1-dodeca-nethiol (DDT) ligands and pushed the peak  $ZT$  value to 2.1 at 932 K. However, bulk materials are usually costly and not suitable for flexible TE devices [29,30].

To date, there has been little attempt at flexible copper-sulfide-based films. For example,  $\text{Cu}_2\text{S}/\text{poly}(3,4\text{-ethylene dioxothiophene}):\text{poly}(\text{styrene sulfonate})$  (PEDOT:PSS) hybrid films were fabricated by screen printing on polyimide. And when the content ratio of  $\text{Cu}_2\text{S}/\text{PEDOT:PSS}$  was 1:1.2, the prepared film showed a maximum PF of  $20.60 \mu\text{W m}^{-1} \text{K}^{-1}$  at  $\sim 400 \text{ K}$  [31]. Self-supporting and flexible  $\text{Cu}_2\text{S}/\text{PEDOT:PSS}$  composite TE films were prepared by a vacuum filtration method, and the maximum PF was  $56.15 \mu\text{W m}^{-1} \text{K}^{-2}$  at 393 K [32]. Both of these films had good flexibility, but the TE performances were low.

Recently, our group [33] reported a one-pot method for the synthesis of  $\text{Ag}_2\text{Se}$  powders combined with vacuum filtration and HP to prepare flexible  $\text{Ag}_2\text{Se}$  film on a nylon membrane, which possessed a PF of  $\sim 2042 \mu\text{W m}^{-1} \text{K}^{-2}$  at RT. This showed that flexible films can be prepared by the above method as long as the size of the powders is beyond the pore size of the nylon membrane. Herein, we designed a green and facile hydrothermal synthesis method to synthesize  $\text{Cu}_{2-x}\text{S}$  powders without any corrosive chemicals and then prepared the  $\text{Cu}_{2-x}\text{S}$  film on nylon membranes by vacuum filtration and then HP. As mentioned above, the  $\sigma$  of  $\text{Cu}_2\text{S}$  is, unfortunately, low. There have been many strategies to improve the  $\sigma$  of TE materials, such as doping to tune carrier concentration ( $n$ ) [27], introducing a second phase with high  $\sigma$  [23], and band engineering [34]. Copper ions in  $\text{Cu}_2\text{S}$  are mobile ions, and doping positive ions with higher electronegativity at the copper site will increase the  $n$  by forming a stronger bond with sulfur and is a good strategy to optimize the electrical properties of  $\text{Cu}_2\text{S}$  [35].

In this work, to improve the PF of the  $\text{Cu}_{2-x}\text{S}$  film, we chose Mn as the dopant to enhance the  $\sigma$  while maintaining the  $\alpha$ . Through the doping of Mn, an optimal film

exhibited a PF of  $113.3 \mu\text{W m}^{-1} \text{K}^{-2}$  at RT, and the output performance of an assembled flexible TE generator (f-TEG) was studied.

## 2. Experimental Section

### 2.1. Sample Synthesis

Mn-doped  $\text{Cu}_{2-x}\text{S}$  powders were synthesized by a hydrothermal method, which was a modified method for  $\text{Cu}_{2-x}\text{S}$  [36]. Typically, 3.6 mmol thiourea (Tu), 7.56 mmol  $\text{CuCl}_2 \cdot 2\text{H}_2\text{O}$ , and  $\text{MnCl}_2 \cdot 4\text{H}_2\text{O}$  were dissolved into 20 mL of deionized (DI) water. The nominal doping content of Mn in  $\text{Cu}_{2-x}\text{S}$  was 0, 1, 3, 5, and 7% by molar ratio, marked as  $\text{Cu}_{2-x}\text{Mn}_y\text{S}$  ( $y = 0, 0.01, 0.03, 0.05, \text{ and } 0.07$ ). Afterward, they were mixed and sonicated for 30 min and then transferred into a 100 mL Teflon-lined stainless-steel autoclave at  $180^\circ\text{C}$  for 18 h with a heating rate of  $2^\circ\text{C min}^{-1}$ . After cooling naturally, the products were washed with DI water and ethanol 3 times. The corresponding films were prepared by vacuum-assisted filtration of the powder dispersions on porous nylon membranes, then dried at  $60^\circ\text{C}$  in vacuum overnight, and, finally, hot-pressed at  $270^\circ\text{C}$  and 1 MPa for 30 min. The schematic diagram of the preparation process of the  $\text{Cu}_{2-x}\text{Mn}_y\text{S}$  film is shown in Figure S1 (see Supplementary Materials).

### 2.2. Assembly of the f-TEG

The  $\text{Cu}_{2-x}\text{Mn}_{0.05}\text{S}$  film was cut into four strips of  $2 \text{ cm} \times 0.5 \text{ cm}$ . Two ends of each strip were coated with a thin layer of Au by evaporation to reduce contact resistance. Then, the four strips were pasted on a polyimide substrate at intervals of 0.5 cm. Finally, Ag paste (SPI#04998-AB) was used to connect the strips in series.

### 2.3. Characterization and Property Measurement

X-ray diffraction (XRD, Bruker D8 Advance,  $\text{Cu K}\alpha$  radiation, Bruker, Shanghai, China) was performed. Scanning electron microscopy (SEM, Nova NanoSEM 450, Thermo Fisher Scientific, Shanghai, China) and energy-dispersive X-ray spectroscopy (EDS) were used to observe the surface and cross-sectional morphology and composition. X-ray photoelectron spectroscopy (XPS, ESALAB 250Xi Spectrometer Microprobe, Thermo Fisher Scientific, Shanghai, China) was used to analyze the composition and valence states of surface elements. The binding energy was calibrated by setting the standard value of C1s to 284.8 eV. Powders scraped from the  $\text{Cu}_{2-x}\text{Mn}_{0.05}\text{S}$  film were observed by transmission electron microscopy (TEM, JEM-2100F, JEOL, Shanghai, China). The films were cut into  $1.3 \text{ cm} \times 0.3 \text{ cm}$  strips to test the temperature dependence of  $\sigma$  and  $\alpha$  with a TE test system (CTA Cryoall, Beijing Cryoall, Shanghai, China) under the protection of He. The Hall carrier concentration ( $n_H$ ) and mobility ( $\mu_H$ ) were measured using the Van der Pauw method with a Hall effect measurement system (HMS-7000, Ecopia, Shanghai, China). To test flexibility,  $\sigma$  was measured before and after bending around a 4 mm-radius rod to test flexibility.

The assembled f-TEG was connected with wires into a circuit, as shown in Figure S2 (see Supplementary Materials) for the output performance test [37,38]. The hot-end temperature was controlled by heating a copper block ( $T + \Delta T$ ) and the other end was put on an adiabatic foam acting as the cold side ( $T$ ). The temperature at both ends was measured by two thermocouples. The output voltage and current were collected by adjusting the variable resistor box at a specific  $\Delta T$ , which was varied by setting different heating temperatures.

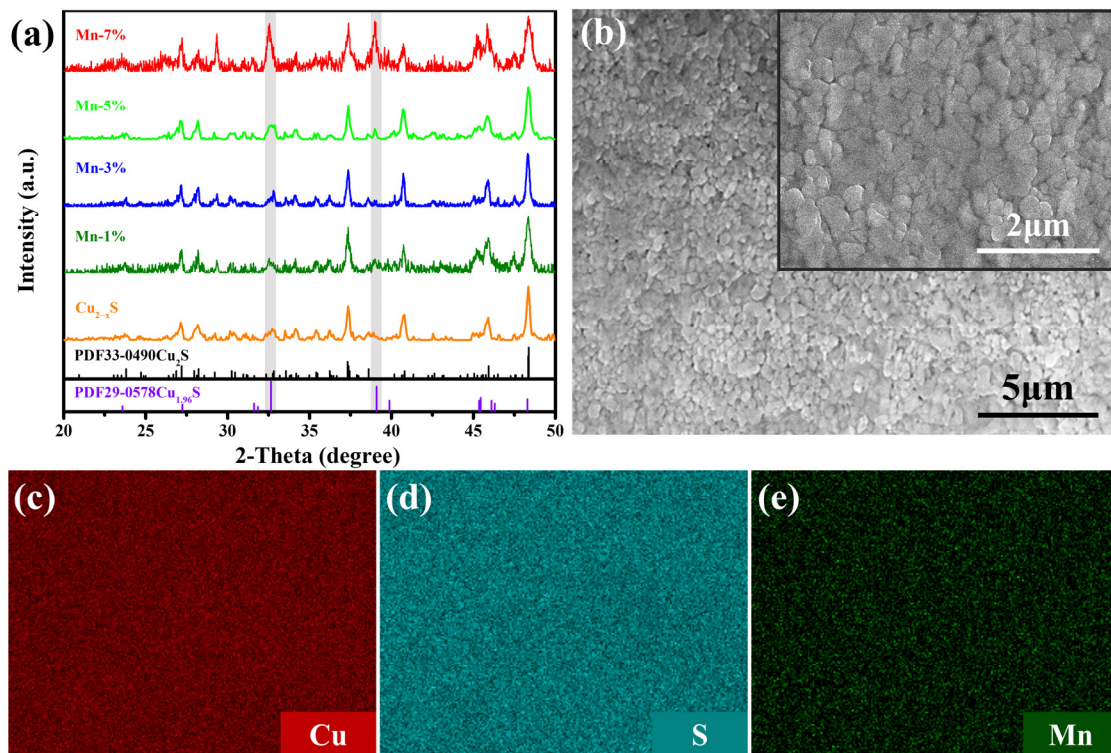
## 3. Results and Discussion

Figure S3 (see Supplementary Materials) shows XRD patterns of the powders. The main phase of undoped copper sulfide can be indexed to tetragonal  $\text{Cu}_2\text{S}$  (PDF No. 72-1071) with evident diffraction peaks at  $2\theta = 31.6^\circ, 32.6^\circ, 39.0^\circ, 39.8^\circ, 45.3^\circ, 46.0^\circ, \text{ and } 48.2^\circ$ , which correspond to (110), (111), (104), (113), (200), (201), and (202) planes of  $\text{Cu}_2\text{S}$ , respectively. There is no obvious shift of XRD peaks and no manganese-related compounds are detected. There are very weak diffraction peaks in Figure S3 when  $y = 0.07$ , which belong to di-

genite  $\text{Cu}_{1.8}\text{S}$  (PDF No. 24-0061). According to [21,36], the related reactions are proposed as follows:



Hydrogen sulfide comes from the decomposition of thiourea in the early stage of the reaction and reacts with copper ions to produce  $\text{CuS}$  [36], which subsequently transforms into  $\text{Cu}_{2-x}\text{S}$  during the heating process [21]. Figure 1a depicts the XRD patterns for the  $\text{Cu}_{2-x}\text{Mn}_y\text{S}$  films. It can be observed that the main diffraction peaks can be well indexed to monoclinic  $\text{Cu}_2\text{S}$  (PDF No. 33-0490). In addition, two peaks at  $2\theta \sim 32.6^\circ$  and  $39.0^\circ$  are detected, corresponding to (103) and (104) planes of tetragonal  $\text{Cu}_{1.96}\text{S}$  (PDF No. 29-0578). Hence, the as-prepared films are composed of  $\text{Cu}_2\text{S}$  with a small amount of  $\text{Cu}_{1.96}\text{S}$ . When the nominal content of Mn is 7%, the XRD peaks for  $\text{Cu}_2\text{S}$  broaden and the peaks for  $\text{Cu}_{1.96}\text{S}$  become stronger.

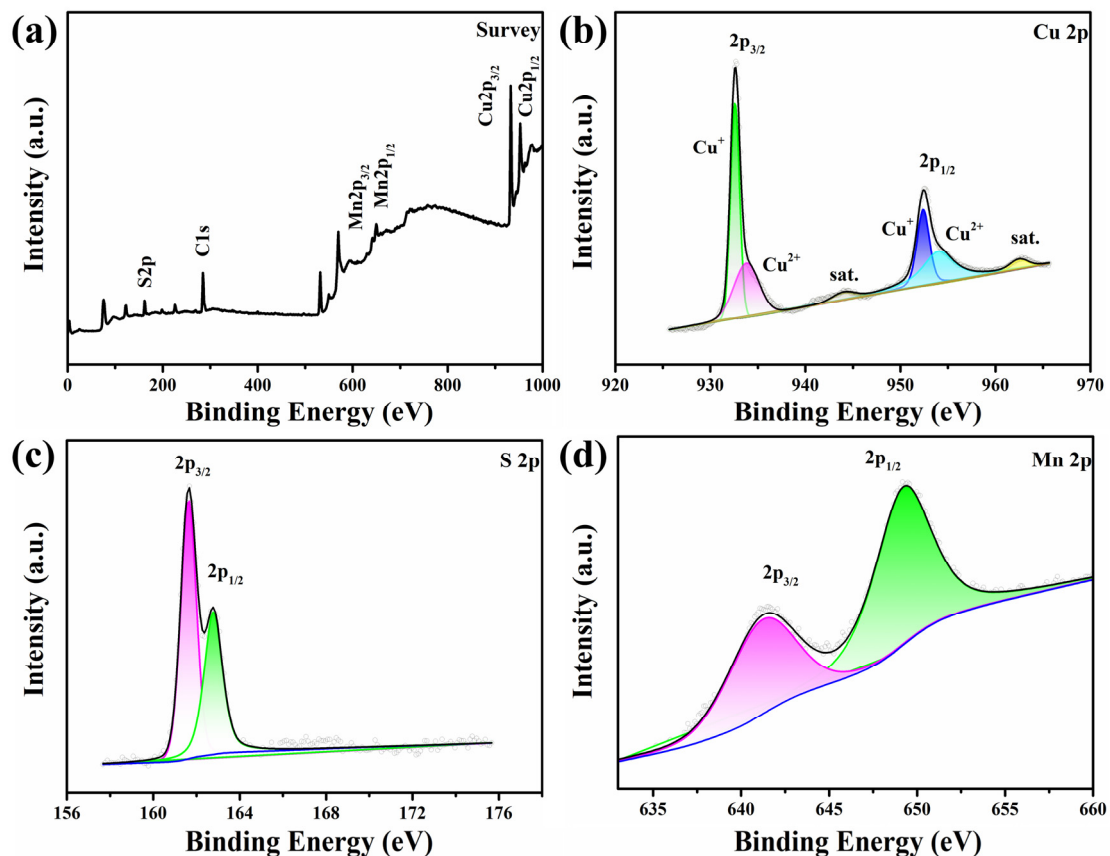


**Figure 1.** (a) XRD patterns of the  $\text{Cu}_{2-x}\text{Mn}_y\text{S}$  films with varying doping content of Mn. (b) A typical SEM image at low magnification, inset at high magnification. (c–e) Corresponding element mappings of the  $\text{Cu}_{2-x}\text{Mn}_{0.05}\text{S}$  film.

Figure S4 (see Supplementary Materials) shows SEM images of  $\text{Cu}_{2-x}\text{Mn}_y\text{S}$  ( $y = 0.01, 0.03, 0.05, \text{ and } 0.07$ ) powders, with most particles being  $\sim 20\text{--}300$  nm. A representative SEM image of the  $\text{Cu}_{2-x}\text{Mn}_{0.05}\text{S}$  film is shown in Figure 1b (the other films show similar morphology, see Supplementary Figure S5). The size of grains is  $< 300$  nm. It can be seen from Figure 1b that the film is not very dense (as the sintering temperature was limited by the melting point of the nylon substrate). EDS results (Figure 1c–e) indicate that the elements of Cu, S, and Mn are homogeneously distributed in the  $\text{Cu}_{2-x}\text{Mn}_{0.05}\text{S}$  film.

Figure 2a shows the XPS survey spectra of the  $\text{Cu}_{2-x}\text{Mn}_{0.05}\text{S}$  film; the signals of Cu, S, Mn, and C are detected. Two strong peaks at 932.6 eV ( $\text{Cu } 2p_{3/2}$ ) and 952.4 eV ( $\text{Cu } 2p_{1/2}$ ) (see Figure 2b) correspond to  $\text{Cu}^+$  [39]. The weak split peaks at about 933.8 and 954.0 eV are attributed to  $\text{Cu}^{2+}$ , and the two satellite peaks located at 944.0 and 962.5 eV also correspond

to  $\text{Cu}^{2+}$  [27,35], which proves the existence of  $\text{Cu}_{1.96}\text{S}$  [40,41]. We estimated the ratio of  $\text{Cu}^+:\text{Cu}^{2+}$  to be about 4.69:1, which is close to the value estimated by semi-quantitative analysis from the XRD result (5.11:1). Compared with the spectra of  $\text{Cu}_{2-x}\text{Mn}_{0.05}\text{S}$  powders (see Supplementary Figure S6), the ratio  $\text{Cu}^+:\text{Cu}^{2+}$  becomes higher, indicating the partial conversion of  $\text{Cu}_{1.96}\text{S}$  to  $\text{Cu}_2\text{S}$  during HP. In Figure 2c, the characteristic peaks of S  $2p_{3/2}$  and  $2p_{1/2}$  are located at 161.6 and 162.8 eV, respectively, and the energy difference between them is about 1.2 eV, indicating the existence of  $\text{S}^{2-}$  [42–44]. Besides, the small resolved peaks with binding energies of 641.2 and 649.2 eV are Mn  $2p_{3/2}$  and  $2p_{1/2}$ , respectively (see Figure 2d). The peak at 641.2 eV of Mn  $2p_{3/2}$  is consistent with the previously reported value of MnS, which is attributed to the Mn-S bond [45]. The XPS and EDS results demonstrate the successful incorporation of Mn into copper sulfide. Mn has an initial valence of +2 and no strong oxidant is present in the reaction, so it is considered that Mn exists in the samples in a divalent state. In addition, because  $\text{Cu}^+$  (0.096 nm) and  $\text{Cu}^{2+}$  (0.072 nm) coexist in the  $\text{Cu}_{2-x}\text{S}$ , while the ionic radius of  $\text{Mn}^{2+}$  (0.080 nm) is between them, the XRD peaks in Figures S3 and 1a have no obvious shift.



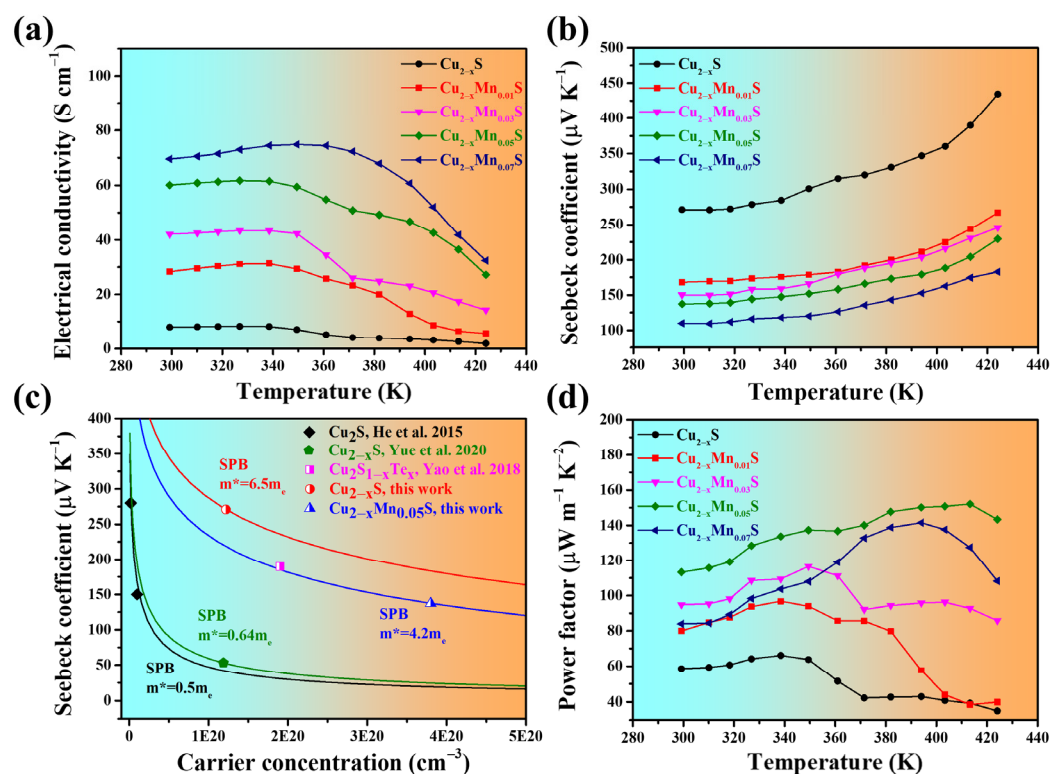
**Figure 2.** XPS spectra of the  $\text{Cu}_{2-x}\text{Mn}_{0.05}\text{S}$  film. (a) Survey scan. (b–d) High-resolution scans for Cu 2p, S 2p, and Mn 2p, respectively.

Figure 3a,b,d show the temperature dependence of TE parameters of the  $\text{Cu}_{2-x}\text{Mn}_y\text{S}$  films. In the initial stage of temperature rise, the  $\sigma$  increases concomitantly, exhibiting a typical semiconductor behavior, and then it decreases when the temperature is near 340 K, which is lower than the transition temperature ( $T_f$ ) of  $\text{Cu}_2\text{S}$  (370 K). The leftward shift of the  $T_f$  is due to the presence of  $\text{Cu}_{1.96}\text{S}$ , which undergoes a phase transition at 336 K [46]. The undoped  $\text{Cu}_{2-x}\text{S}$  film possessed a high  $\alpha$  of  $271 \mu\text{V K}^{-1}$  and a low  $\sigma$  of  $8 \text{ S cm}^{-1}$  at RT. As the Mn doping amount increased, the  $\sigma$  increased, reaching  $\sim 70 \text{ S cm}^{-1}$  when  $y = 0.07$ , nearly nine times as high as that of the undoped  $\text{Cu}_{2-x}\text{S}$  film.  $\text{Cu}_{2-x}\text{S}$  is a type of p-type semiconductor (see hereinafter). Manganese was doped into copper sulfide in the form of

divalent ions, according to the XPS analysis, which should provide additional electrons in the  $\text{Cu}_{2-x}\text{Mn}_y\text{S}$  films to act as a donor. However, the  $\sigma$  at RT exhibited an opposite trend. This phenomenon is consistent with the change in  $\sigma$  of Mn- and Sn-alloyed  $\text{Cu}_2\text{S}$  bulk obtained by the melting method [39]. Besides, through molecular orbital theory analysis, Wang et al. [47] revealed that the 3d orbital energies of Mn were similar to those of S 3p orbitals, causing the S 3p orbital to move away from the Cu-S bond, thereby weakening the Cu-S bond. Hence, the introduction of Mn weakens the Cu-S chemical bond, resulting in the formation of more Cu vacancies in the crystal lattice [39,48,49], namely, increasing the hole concentrations, which agrees with the Hall test result: At RT, the  $n_H$  increased from  $1.22 \times 10^{20}$  for the  $\text{Cu}_{2-x}\text{S}$  and to  $3.80 \times 10^{20} \text{ cm}^{-3}$  for the  $\text{Cu}_{2-x}\text{Mn}_{0.05}\text{S}$ . In addition, the  $\mu_H$  also increased from 2.91 for the  $\text{Cu}_{2-x}\text{S}$  to  $4.37 \text{ cm}^2 \text{ V}^{-1} \text{ s}^{-1}$  for the  $\text{Cu}_{2-x}\text{Mn}_{0.05}\text{S}$ . Since the  $\sigma$  is proportional to the  $n$  and mobility ( $\mu$ ), defined as:

$$\sigma = nq\mu \quad (4)$$

where  $q$  is the electron charge, the  $\sigma$  of the  $\text{Cu}_{2-x}\text{Mn}_{0.05}\text{S}$  film was ultimately improved.



**Figure 3.** The temperature-dependent (a) electrical conductivities and (b) Seebeck coefficients. (c) Seebeck coefficient as a function of carrier concentration for  $\text{Cu}_{2-x}\text{S}$ -,  $\text{Cu}_{2-x}\text{Mn}_{0.05}\text{S}$ -, and reported  $\text{Cu}_{2-x}\text{S}$ -based bulks [21,50,51] at 300 K. (d) Temperature-dependent power factors of the  $\text{Cu}_{2-x}\text{Mn}_y\text{S}$  films.

The  $\alpha$  increased with rising temperature (Figure 3b). And the positive  $\alpha$  values also indicate that holes were the dominant charge carriers. As the Mn doping amount increased, the  $\alpha$  decreased from 271 to  $109.9 \mu\text{V K}^{-1}$  at RT, which is opposite to the trend of  $\sigma$  with the amount of doping. The  $\alpha$  is proportional to  $n^{-2/3}$ , expressed as follows:

$$\alpha = \frac{8\pi^2 k_B^2}{3eh^2} m^* T \left( \frac{\pi}{3n} \right)^{2/3} \quad (5)$$

where  $k_B$  is the Boltzmann constant,  $h$  is the Planck constant, and  $m^*$  is the effective mass of carriers. Therefore, an increase in  $n$  will lead to a decrease in  $\alpha$ . Figure 3c gives the  $\alpha$  as

a function of  $n$  based on a single parabolic band (SPB) model and assuming a dominated scattering by acoustic phonons, which is called the Pisarenko curve. The  $m^*$  of  $\text{Cu}_{2-x}\text{S}$  in this work (the red line) is  $6.5 m_e$ . It is much higher than that of the reported data for  $\text{Cu}_2\text{S}$  ( $0.5 m_e$ ) bulk [50]. In ref. [50], the  $\alpha$  of the  $\text{Cu}_2\text{S}$  is  $280 \mu\text{V K}^{-1}$  with  $n_H \sim 2.3 \times 10^{18} \text{ cm}^{-3}$ , whereas the  $\alpha$  of the present  $\text{Cu}_{2-x}\text{S}$  is  $271 \mu\text{V K}^{-1}$  with  $n_H \sim 1.22 \times 10^{20} \text{ cm}^{-3}$ . According to Equation (5), the  $\text{Cu}_{2-x}\text{S}$  will have a much higher  $m^*$ . Therefore, the  $\text{Cu}_{2-x}\text{S}$  with a large  $m^*$  is due to it having a high  $n_H$ . In the present case, the  $\text{Cu}_{2-x}\text{S}$  consisted of two phases:  $\text{Cu}_2\text{S}$  and  $\text{Cu}_{1.96}\text{S}$ . The  $\text{Cu}_{1.96}\text{S}$ , which possesses more copper vacancies, would have increased the  $n_H$  [28,52]. And manganese doping ( $y = 0.05$ ) effectively reduced the  $m^*$  to  $4.2 m_e$ , which is close to the value of  $\text{Cu}_2\text{S}_{1-x}\text{Te}_x$  [51] ( $m^* = 4.5 m_e$ ). Consequently, a higher  $n$  and reduced  $m^*$  adjusted the  $\alpha$  to a moderate value. Additionally, the decreased  $m^*$  also had an impact on  $\mu$  according to the equation:

$$\mu = \frac{q\tau}{m^*} \quad (6)$$

where  $\tau$  is the carrier relaxation time. The decrease in  $m^*$  caused the enhancement of  $\mu$  after doping. As a result, the  $\text{Cu}_{2-x}\text{Mn}_y\text{S}$  ( $y = 0.05$ ) film possessed a higher PF of  $\sim 113.3 \mu\text{W m}^{-1} \text{ K}^{-2}$  at RT ( $\sim 152.1 \mu\text{W m}^{-1} \text{ K}^{-2}$  at 413 K), nearly twice that of the  $\text{Cu}_{2-x}\text{S}$  film ( $58.5 \mu\text{W m}^{-1} \text{ K}^{-2}$ ). Table 1 shows a comparison of TE performance between this work and the reported copper-sulfide-based bulks and flexible films. The PF value of the  $\text{Cu}_{2-x}\text{Mn}_{0.05}\text{S}$  film was superior to those of previously reported  $\text{Cu}_2\text{S}$ -based flexible films and most bulks. However, it was lower than the PF value in ref. [21]. This may have been due to the fact that the  $\text{Cu}_{2-x}\text{Mn}_{0.05}\text{S}$  film was relatively porous compared to the SPS sintered bulk.

**Table 1.** TE performance of the reported copper-sulfide-based bulks and flexible films.

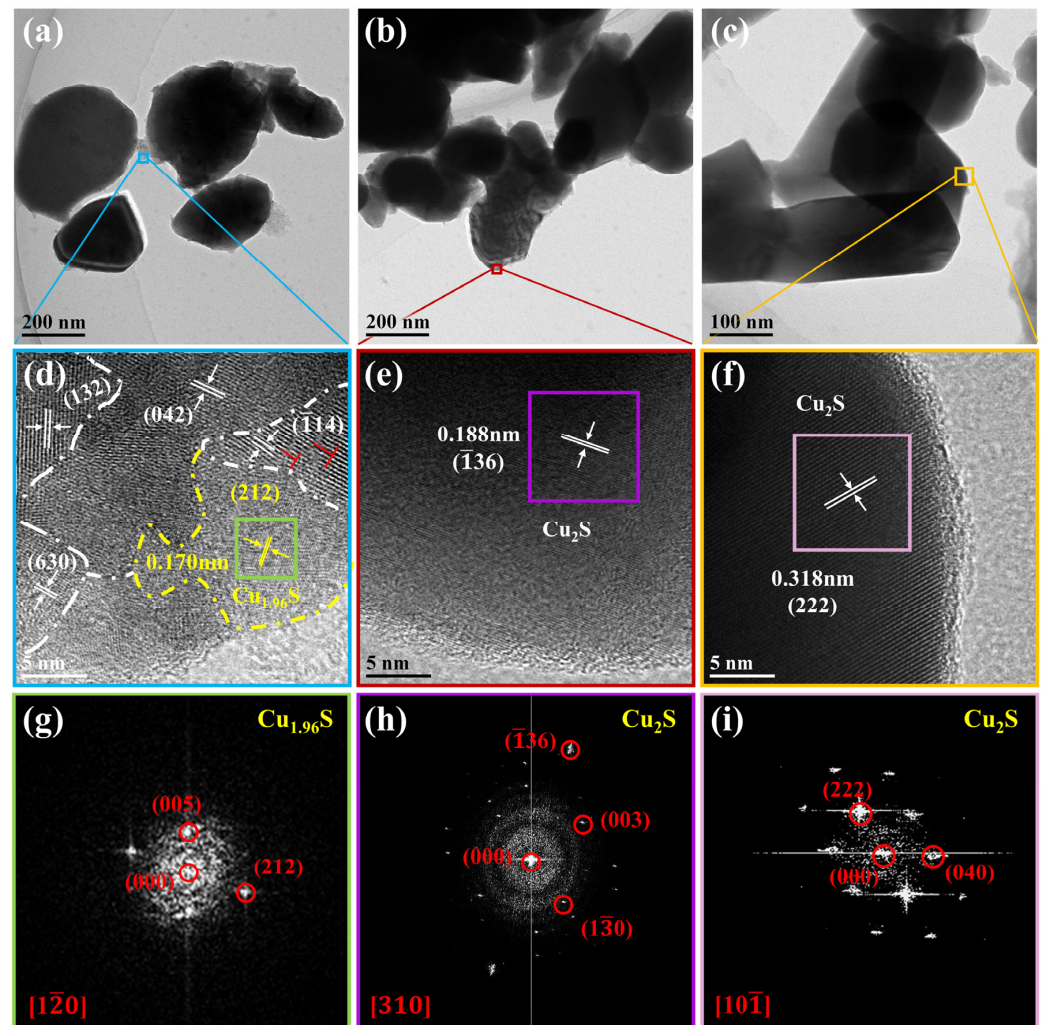
Materials	PF ( $\mu\text{W m}^{-1} \text{ K}^{-2}$ )	Temperature (K)	Method	Ref. No
$\text{Cu}_{2-x}\text{S}$	56	300	Solvothermal and HP	[52]
$\text{Cu}_{2-x}\text{S}$	75	300	Melting and SPS	[53]
$\text{Cu}_{1.98-2x}\text{Mn}_x\text{S}_{0.985}\text{Se}_{0.015}$	100	325	Melting and SPS	[47]
$\text{Cu}_2\text{S}_{1-x}\text{Se}_x$	122	325	Ball milling and SPS	[24]
Micro/nano $\text{Cu}_{2-x}\text{S}$	250	320	Hydrothermal and SPS	[21]
$\text{Cu}_2\text{S}_{1-x}\text{Te}_x$	145	325	Ball milling and SPS	[54]
$\text{Cu}_2\text{S}$ hybrid films	20	393	Screen printing	[31]
$\text{Cu}_2\text{S}/\text{PEDOT:PSS}$ films	56	393	Vacuum filtration	[32]
$\text{Cu}_{2-x}\text{Mn}_y\text{S}/\text{nylon}$ films	113	300	Hydrothermal and HP	This work
	150	393		

Note: The data related to copper-sulfide-based bulks are estimated from the relevant reported graphs.

To further understand the internal microstructure, TEM was applied for observation of the grains scraped from the optimal film, and the result is shown in Figure 4. The grain sizes were  $\sim 20\text{--}300$  nm. In the HRTEM image (Figure 4d), the measured lattice spacings of 0.305, 0.266, 0.315, and 0.194 nm are in good agreement with those of the (132), (042), ( $-114$ ), and (630) planes of monoclinic  $\text{Cu}_2\text{S}$ , respectively. And there are edge dislocations in the grains, which may be the lattice distortion caused by Mn doping. In addition,  $\text{Cu}_{1.96}\text{S}$  is observed. Figure 4g shows an FFT image of the grain circled in a yellow dotted line, and the interplanar spacing is about 0.170 nm, corresponding to that of the (212) plane of  $\text{Cu}_{1.96}\text{S}$  [52]. Figure 4e,f,h,i demonstrate that the lattice spacings are 0.188 and 0.318 nm, which correspond to the ( $-136$ ) and (222) planes of  $\text{Cu}_2\text{S}$ . Thus, the TEM results also confirm that the  $\text{Cu}_{2-x}\text{Mn}_{0.05}\text{S}$  film contained two the phases,  $\text{Cu}_2\text{S}$  and  $\text{Cu}_{1.96}\text{S}$ .

Flexibility is also a key factor in the practical application of f-TEFs. The thickness of the  $\text{Cu}_{2-x}\text{Mn}_{0.05}\text{S}$  film was approximately  $8.96 \mu\text{m}$  (see Supplementary Figure S7). And Figure 5a shows the corresponding flexibility test result: the  $\sigma$  maintained at 94.4%, 93.3%, and 89.6% of the original after being bent around a 4 mm-radius rod 500, 1000, and 1500 times, respectively. This is better than the flexibility of the reported  $\text{Cu}_2\text{S}/\text{PEDOT:PSS}$

composite films [32] (the resistance rose 10% after bending 1000 cycles under a bending radius of 4 mm). The main reasons for the good flexibility are as follows: (1) the nylon membrane possessed excellent flexibility and (2) the combination between the porous film and the nylon membrane was good (see Figure 5b).



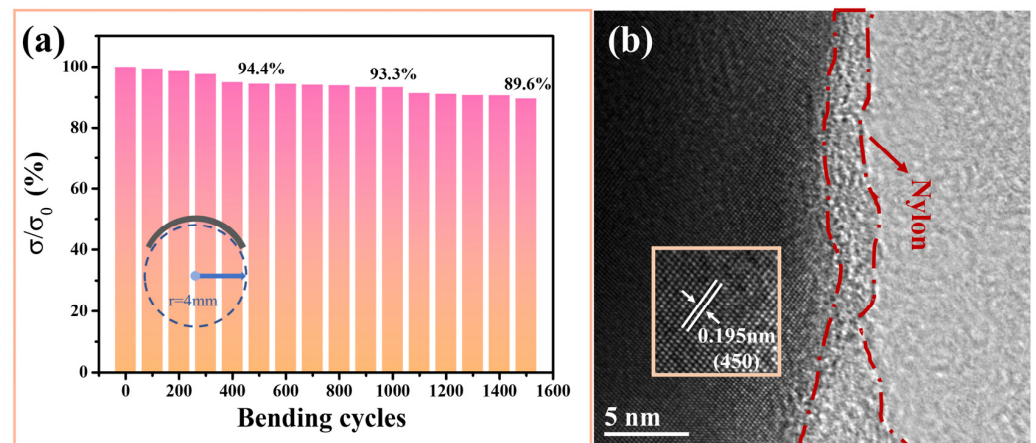
**Figure 4.** Microstructure characterization of grains scraped from the  $\text{Cu}_{2-x}\text{Mn}_{0.05}\text{S}$  film. (a–c) TEM images. (d–f) Enlarged images of the blue, red, and orange squares marked in (a–c), respectively. The “ $\perp$ ” in (d) denotes edge dislocation. (g–i) FFT images corresponding to the grains marked with green, purple, and pink squares in (d–f), respectively.

Figure 6a gives the variation of open-circuit voltage ( $V_{oc}$ ) with  $\Delta T$ . When the  $\Delta T$  values were 10.3, 21.3, and 30.1 K, the  $V_{oc}$  values of the f-TEG were 5.74, 11.86, and 16.65 mV, respectively, which is close to the values (see Figure 6c) calculated by the equation:  $V_{oc} = |\alpha| \cdot N \cdot \Delta T$  ( $N$  is the number of f-TEG legs). Figure 6b shows the output properties of the f-TEG by adjusting the load resistance ( $R_{load}$ ) under different  $\Delta T$ . Output voltage ( $V_{out}$ ) and output current ( $I_{out}$ ) show a negative correlation. The output power ( $P_{out}$ ) of the f-TEG can be calculated by the equation below:

$$P_{out} = \frac{V_{out}^2}{R_{in} + R_{ex}} \quad (7)$$

where  $R_{in}$  is the internal resistance of the f-TEG,  $R_{ex}$  includes  $R_{load}$  and  $R_{box+ammeter}$  ( $\sim 15.7 \Omega$ , the internal resistance of the variable resistance box and the ammeter).  $R_{in}$  was measured to be  $264 \Omega$ , and the resistance of the four legs ( $R_1$ ) was calculated by the formula

$R_1 = N \cdot l / \sigma \cdot A$  is  $249 \Omega$  ( $l$  and  $A$  are the length and cross-sectional area of one leg). Their difference comes from the contact resistance of the f-TEG. When  $R_{in}$  was equal to  $R_{ex}$ , the  $P_{out}$  reached its maximum value ( $P_{max}$ ). At  $\Delta T$  values of 10.3, 21.3, and 30.1 K, the  $P_{max}$  values were about 29.92, 123.87, and 249.48 nW, respectively, corresponding to  $R_{load}$  of  $\sim 251 \Omega$ . Therefore,  $R_{ex} = R_{load} + R_{box+ammeter} = \sim 251 \Omega + 15.7 \Omega = \sim 266.7 \Omega$ , close to the  $R_{in}$  ( $264 \Omega$ ). The measured  $P_{max}$  value was close to the value estimated by the equation:  $P_{max} = V_{oc}^2 / 4R_{in}$  (see Figure 6d; more details are shown in Supplementary Table S1). The maximum power density ( $PD_{max}$ ) can be obtained by dividing  $P_{max}$  by the total cross-sectional area of the f-TEG. It was  $1.23 \text{ W m}^{-2}$  at a  $\Delta T$  of 30.1 K, which indicates that this f-TEG has a good potential for powering low-power consumption wearable electronics.



**Figure 5.** (a) Flexibility of the  $\text{Cu}_{2-x}\text{Mn}_{0.05}\text{S}$  film: The relative electrical conductivity changes with bending around a bending radius of 4 mm. (b) An HRTEM image of the  $\text{Cu}_{2-x}\text{Mn}_{0.05}\text{S}$  film showing a good combination between the film and the nylon membrane; the inset is the corresponding IFFT image.

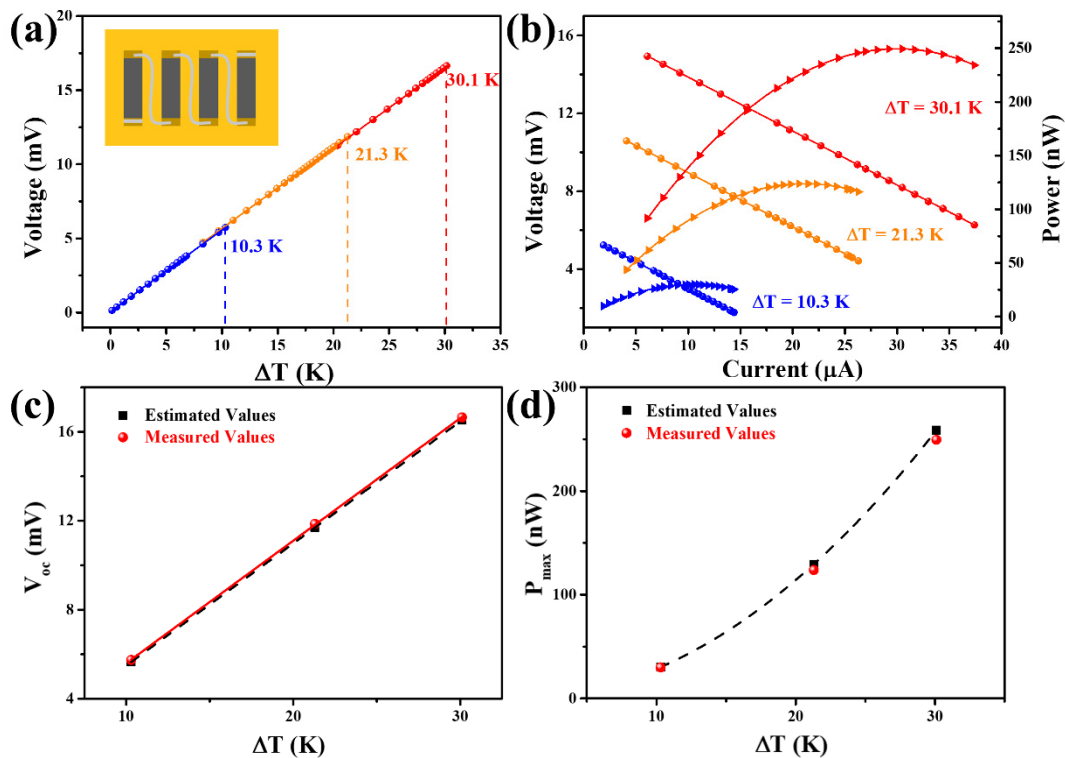


**Figure 6.** Output performance of the f-TEG assembled with the  $\text{Cu}_{2-x}\text{Mn}_{0.05}\text{S}$  film. (a) The open-circuit voltage at different  $\Delta T$  (the inset is a schematic diagram of the four-leg f-TEG). (b) Output voltage and

power versus current at different  $\Delta T$ . The straight lines and curves in (b) correspond to V-I and P-I relations, respectively. Comparison of the estimated and measured values of the (c) open circuit voltage ( $V_{oc}$ ) and (d) maximum output power ( $P_{max}$ ) under different  $\Delta T$ .

#### 4. Conclusions

In summary, we synthesized a series of Mn-doped  $\text{Cu}_{2-x}\text{S}$  powders by a green and facile hydrothermal method and successfully prepared Mn-doped  $\text{Cu}_{2-x}\text{S}$ /nylon flexible films. The doping of Mn increased the  $n$  and  $\mu$ , which ultimately improved the  $\sigma$  of the  $\text{Cu}_{2-x}\text{Mn}_y\text{S}$  films. The optimal film ( $\text{Cu}_{2-x}\text{Mn}_{0.05}\text{S}$ ) exhibited a high PF of  $113.3 \mu\text{W m}^{-1} \text{K}^{-2}$  at RT, with an enhanced  $\sigma$  of  $60.1 \text{ S cm}^{-1}$  and a proper  $\alpha$  of  $137.3 \mu\text{V K}^{-1}$ . At the same time, this film possessed good flexibility: the  $\sigma$  was maintained at  $\sim 93.3\%$  after bending 1000 times around a rod with a radius of 4 mm. An assembled four-leg f-TEG produced a maximum power of 249.48 nW (corresponding power density  $\sim 1.23 \text{ W m}^{-2}$ ) at a  $\Delta T$  of 30.1 K. Our results indicate that Mn doping is an effective and convenient to improve the electrical properties of  $\text{Cu}_{2-x}\text{S}$  and provides the possibility of fabricating low-cost and high-flexibility copper-sulfide-based films for powering wearable devices.

**Supplementary Materials:** The following supporting information can be downloaded at: <https://www.mdpi.com/article/10.3390/ma16227159/s1>. Figure S1: Schematic diagram of the preparation process of the  $\text{Cu}_{2-x}\text{Mn}_y\text{S}$  film; Figure S2: A schematic diagram for the output performance measurement of the TE generator; Figure S3: XRD patterns of the  $\text{Cu}_{2-x}\text{Mn}_y\text{S}$  powders with varying doping content of Mn; Figure S4: SEM images of  $\text{Cu}_{2-x}\text{Mn}_y\text{S}$  powders. (a)  $y = 0.01$ , (b)  $y = 0.03$ , (c)  $y = 0.05$ , (d)  $y = 0.07$ ; Figure S5: SEM images of the  $\text{Cu}_{2-x}\text{Mn}_y\text{S}$  films. (a)  $y = 0.01$ , (b)  $y = 0.03$ , (c)  $y = 0.05$ , (d)  $y = 0.07$ ; Figure S6: XPS spectra of the  $\text{Cu}_{2-x}\text{Mn}_{0.05}\text{S}$  powders. (a) survey scan. (b–d) high-resolution scans for Cu 2p, S 2p and Mn 2p, respectively; Figure S7: Cross-sectional SEM image of the  $\text{Cu}_{2-x}\text{Mn}_{0.05}\text{S}$  film; Table S1. The measured and estimated values of the open-circuit voltage ( $V_{oc}$ ) and maximum output power ( $P_{max}$ ) of the f-TEG at different  $\Delta T$ .

**Author Contributions:** Conceptualization, K.C.; Methodology, X.Z.; Formal analysis, X.Z., X.H., Y.L. (Yiming Lu), Y.L. (Ying Liu), Z.W. and J.L.; Investigation, X.Z.; Writing—original draft, X.Z.; Writing—review & editing, X.H., Y.L. (Yiming Lu), Y.L. (Ying Liu), Z.W., J.L. and K.C.; Supervision, K.C.; Project administration, K.C. All authors have read and agreed to the published version of the manuscript.

**Funding:** This work was supported by the National Natural Science Foundation of China (51972234 and 92163118).

**Institutional Review Board Statement:** Not applicable.

**Informed Consent Statement:** Not applicable.

**Data Availability Statement:** Data are contained within the article and Supplementary Materials.

**Conflicts of Interest:** The authors declare that they have no conflict of interest.

#### References

1. Bell, L.E. Cooling, heating, generating power, and recovering waste heat with thermoelectric systems. *Science* **2008**, *321*, 1457–1461. [[CrossRef](#)]
2. Wang, Y.; Shi, Y.; Mei, D.; Chen, Z. Wearable thermoelectric generator to harvest body heat for powering a miniaturized accelerometer. *Appl. Energy* **2018**, *215*, 690–698. [[CrossRef](#)]
3. Zebarjadi, M.; Esfarjani, K.; Dresselhaus, M.S.; Ren, Z.F.; Chen, G. Perspectives on thermoelectrics: From fundamentals to device applications. *Energy Environ. Sci.* **2012**, *5*, 5147–5162. [[CrossRef](#)]
4. Fan, J.; Huang, X.; Liu, F.; Deng, L.; Chen, G. Feasibility of using chemically exfoliated SnSe nanobelts in constructing flexible SWCNTs-based composite films for high-performance thermoelectric applications. *Compos. Commun.* **2021**, *24*, 100612. [[CrossRef](#)]
5. Park, W.; Park, S.; Mun, Y.; Lee, D.; Jang, K.-S. Effects of thickness on flexibility and thermoelectric performance of free-standing  $\text{Ag}_2\text{Se}$  films. *J. Ind. Eng. Chem.* **2023**, *121*, 142–148. [[CrossRef](#)]
6. Wang, L.; Zhang, Z.; Liu, Y.; Wang, B.; Fang, L.; Qiu, J.; Zhang, K.; Wang, S. Exceptional thermoelectric properties of flexible organic–inorganic hybrids with monodispersed and periodic nanophase. *Nat. Commun.* **2018**, *9*, 3817. [[CrossRef](#)]

7. Ding, Y.; Qiu, Y.; Cai, K.; Yao, Q.; Chen, S.; Chen, L.; He, J. High performance n-type Ag<sub>2</sub>Se film on nylon membrane for flexible thermoelectric power generator. *Nat. Commun.* **2019**, *10*, 841. [[CrossRef](#)]
8. Howlader, S.; Vasudevan, R.; Jarwal, B.; Gupta, S.; Chen, K.H.; Sachdev, K.; Banerjee, M.K. Microstructure and mechanical stability of Bi doped Mg<sub>2</sub>Si<sub>0.4</sub>Sn<sub>0.6</sub> thermoelectric material. *J. Alloys Compd.* **2020**, *818*, 15288. [[CrossRef](#)]
9. Varghese, T.; Dun, C.; Kempf, N.; Saeidi-Javash, M.; Karthik, C.; Richardson, J.; Hollar, C.; Estrada, D.; Zhang, Y. Flexible Thermoelectric Devices of Ultrahigh Power Factor by Scalable Printing and Interface Engineering. *Adv. Funct. Mater.* **2019**, *30*, 5796. [[CrossRef](#)]
10. Shang, H.; Dun, C.; Deng, Y.; Li, T.; Gao, Z.; Xiao, L.; Gu, H.; Singh, D.J.; Ren, Z.; Ding, F. Bi<sub>0.5</sub>Sb<sub>1.5</sub>Te<sub>3</sub>-based films for flexible thermoelectric devices. *J. Mater. Chem. A* **2020**, *8*, 4552–4561. [[CrossRef](#)]
11. Gao, J.; Miao, L.; Liu, C.; Wang, X.; Peng, Y.; Wei, X.; Zhou, J.; Chen, Y.; Hashimoto, R.; Asaka, T.; et al. A novel glass-fiber-aided cold-press method for fabrication of n-type Ag<sub>2</sub>Te nanowires thermoelectric film on flexible copy-paper substrate. *J. Mater. Chem. A* **2017**, *5*, 24740–24748. [[CrossRef](#)]
12. Li, X.; Cai, K.; Gao, M.; Du, Y.; Shen, S. Recent advances in flexible thermoelectric films and devices. *Nano Energy* **2021**, *89*, 106309. [[CrossRef](#)]
13. Fan, Z.; Du, D.; Guan, X.; Ouyang, J. Polymer films with ultrahigh thermoelectric properties arising from significant seebeck coefficient enhancement by ion accumulation on surface. *Nano Energy* **2018**, *51*, 481–488. [[CrossRef](#)]
14. Wang, H.; Hsu, J.H.; Yi, S.L.; Kim, S.L.; Choi, K.; Yang, G.; Yu, C. Thermally Driven Large N-Type Voltage Responses from Hybrids of Carbon Nanotubes and Poly(3,4-ethylenedioxythiophene) with Tetrakis(dimethylamino)ethylene. *Adv. Mater.* **2015**, *27*, 6855–6861. [[CrossRef](#)] [[PubMed](#)]
15. Fan, W.; Guo, C.; Chen, G. Flexible films of poly(3,4-ethylenedioxythiophene)/carbon nanotube thermoelectric composites prepared by dynamic 3-phase interfacial electropolymerization and subsequent physical mixing. *J. Mater. Chem. A* **2018**, *6*, 12275–12280. [[CrossRef](#)]
16. Jiang, C.; Wei, P.; Ding, Y.; Cai, K.; Tong, L.; Gao, Q.; Lu, Y.; Zhao, W.; Chen, S. Ultrahigh performance polyvinylpyrrolidone/Ag<sub>2</sub>Se composite thermoelectric film for flexible energy harvesting. *Nano Energy* **2021**, *80*, 105488. [[CrossRef](#)]
17. Li, Y.; Lou, Q.; Yang, J.; Cai, K.; Liu, Y.; Lu, Y.; Qiu, Y.; Lu, Y.; Wang, Z.; Wu, M.; et al. Exceptionally High Power Factor Ag<sub>2</sub>Se/Se/Polypyrrole Composite Films for Flexible Thermoelectric Generators. *Adv. Funct. Mater.* **2021**, *32*, 216902. [[CrossRef](#)]
18. Wang, Z.; Gao, Q.; Wang, W.; Lu, Y.; Cai, K.; Li, Y.; Wu, M.; He, J. High performance Ag<sub>2</sub>Se/Ag/PEDOT composite films for wearable thermoelectric power generators. *Mater. Today Phys.* **2021**, *21*, 100553. [[CrossRef](#)]
19. Lei, Y.; Qi, R.; Chen, M.; Chen, H.; Xing, C.; Sui, F.; Gu, L.; He, W.; Zhang, Y.; Baba, T.; et al. Microstructurally Tailored Thin beta-Ag<sub>2</sub>Se Films toward Commercial Flexible Thermoelectrics. *Adv. Mater.* **2022**, *34*, 2104786. [[CrossRef](#)]
20. Mulla, R.; Rabinal, M.H.K. Copper Sulfides: Earth-Abundant and Low-Cost Thermoelectric Materials. *Energy Technol.* **2019**, *7*, 1800850. [[CrossRef](#)]
21. Yue, Z.; Zhou, W.; Ji, X.; Wang, Y.; Guo, F. Thermoelectric performance of hydrothermally synthesized micro/nano Cu<sub>2</sub>-xS. *Chem. Eng. J.* **2022**, *449*, 137748. [[CrossRef](#)]
22. He, Y.; Day, T.; Zhang, T.; Liu, H.; Shi, X.; Chen, L.; Snyder, G.J. High thermoelectric performance in non-toxic earth-abundant copper sulfide. *Adv. Mater.* **2014**, *26*, 3974–3978. [[CrossRef](#)] [[PubMed](#)]
23. Zhao, L.; Wang, X.; Fei, F.Y.; Wang, J.; Cheng, Z.; Dou, S.; Wang, J.; Snyder, G.J. High thermoelectric and mechanical performance in highly dense Cu<sub>2</sub>-xS bulks prepared by a melt-solidification technique. *J. Mater. Chem. A* **2015**, *3*, 9432–9437. [[CrossRef](#)]
24. Yao, Y.; Zhang, B.P.; Pei, J.; Liu, Y.C.; Li, J.F. Thermoelectric performance enhancement of Cu<sub>2</sub>S by Se doping leading to a simultaneous power factor increase and thermal conductivity reduction. *J. Mater. Chem. C* **2017**, *5*, 7845–7852. [[CrossRef](#)]
25. Chakrabarti, D.J.; Laughlin, D.E. The Cu-S (Copper-Sulfur) System. *Bull. Alloys Phase Diagr.* **1983**, *4*, 254. [[CrossRef](#)]
26. Tang, H.C.; Sun, F.H.; Dong, J.F.; Asfandiyar; Zhuang, H.L.; Pan, Y.; Li, J.F. Graphene network in copper sulfide leading to enhanced thermoelectric properties and thermal stability. *Nano Energy* **2018**, *49*, 267–273. [[CrossRef](#)]
27. Yue, Z.; Zhou, W.; Ji, X.; Zhang, F.; Guo, F. Enhanced thermoelectric properties of Ag doped Cu<sub>2</sub>S by using hydrothermal method. *J. Alloys Compd.* **2022**, *919*, 165830. [[CrossRef](#)]
28. Li, X.; Lou, Y.; Jin, K.; Fu, L.; Xu, P.; Shi, Z.; Feng, T.; Xu, B. Realizing zT>2 in Environment-Friendly Monoclinic Cu<sub>2</sub>S—Tetragonal Cu<sub>1.96</sub>S Nano-Phase Junctions for Thermoelectrics. *Angew. Chem. Int. Ed.* **2022**, *61*, e202212885. [[CrossRef](#)]
29. Zhang, Q.H.; Huang, X.Y.; Bai, S.Q.; Shi, X.; Uher, C.; Chen, L.D. Thermoelectric Devices for Power Generation: Recent Progress and Future Challenges. *Adv. Eng. Mater.* **2016**, *18*, 194–213. [[CrossRef](#)]
30. Jaziri, N.; Boughamoura, A.; Müller, J.; Mezghani, B.; Tounsi, F.; Ismail, M. A comprehensive review of Thermoelectric Generators: Technologies and common applications. *Energy Rep.* **2020**, *6*, 264–287. [[CrossRef](#)]
31. Zhao, J.; Zhao, X.; Guo, R.; Zhao, Y.; Yang, C.; Zhang, L.; Liu, D.; Ren, Y. Preparation and Characterization of Screen-Printed Cu(2S)/PEDOT:PSS Hybrid Films for Flexible Thermoelectric Power Generator. *Nanomaterials* **2022**, *12*, 2430. [[CrossRef](#)] [[PubMed](#)]
32. Liu, D.; Yan, Z.; Zhao, Y.; Zhang, Z.; Zhang, B.; Shi, P.; Xue, C. Facile self-supporting and flexible Cu<sub>2</sub>S/PEDOT:PSS composite thermoelectric film with high thermoelectric properties for body energy harvesting. *Results Phys.* **2021**, *31*. [[CrossRef](#)]
33. Liu, Y.; Lu, Y.; Wang, Z.; Li, J.; Wei, P.; Zhao, W.; Chen, L.; Cai, K. High performance Ag<sub>2</sub>Se films by a one-pot method for a flexible thermoelectric generator. *J. Mater. Chem. A* **2022**, *10*, 25644–25651. [[CrossRef](#)]
34. Lee, K.H.; Kim, S.-i.; Kim, H.-S.; Kim, S.W. Band Convergence in Thermoelectric Materials: Theoretical Background and Consideration on Bi–Sb–Te Alloys. *ACS Appl. Energy Mater.* **2020**, *3*, 2214–2223. [[CrossRef](#)]

35. Peng, Q.; Zhang, S.; Yang, H.; Sheng, B.; Xu, R.; Wang, Q.; Yu, Y. Boosting Potassium Storage Performance of the Cu<sub>2</sub>S Anode via Morphology Engineering and Electrolyte Chemistry. *ACS Nano* **2020**, *14*, 6024–6033. [[CrossRef](#)]
36. Tao, F.; Zhang, Y.; Zhang, F.; An, Y.; Dong, L.; Yin, Y. Structural evolution from CuS nanoflowers to Cu<sub>9</sub>S<sub>5</sub> nanosheets and their applications in environmental pollution removal and photothermal conversion. *RSC Adv.* **2016**, *6*, 63820–63826. [[CrossRef](#)]
37. Nandihalli, N. A short account of thermoelectric film characterization techniques. *Mater. Today Phys.* **2023**, *36*, 101173. [[CrossRef](#)]
38. Wang, C.; Chen, F.; Sun, K.; Chen, R.; Li, M.; Zhou, X.; Sun, Y.; Chen, D.; Wang, G. Contributed Review: Instruments for measuring Seebeck coefficient of thin film thermoelectric materials: A mini-review. *Rev. Sci. Instrum.* **2018**, *89*, 5038406. [[CrossRef](#)]
39. Nkemeni, D.S.; Yang, Z.; Lou, S.; Li, G.; Zhou, S. Achievement of extra-high thermoelectric performance in doped copper (I) sulfide. *J. Alloys Compd.* **2021**, *878*, 160128. [[CrossRef](#)]
40. Wu, R.; Wang, D.P.; Kumar, V.; Zhou, K.; Law, A.W.; Lee, P.S.; Lou, J.; Chen, Z. MOFs-derived copper sulfides embedded within porous carbon octahedra for electrochemical capacitor applications. *Chem. Commun.* **2015**, *51*, 3109–3112. [[CrossRef](#)]
41. Jia, X.; Zhang, E.; Yu, X.; Lu, B. Facile Synthesis of Copper Sulfide Nanosheet@Graphene Oxide for the Anode of Potassium-Ion Batteries. *Energy Technol.* **2019**, *8*, 1900987. [[CrossRef](#)]
42. Geng, X.; Jiao, Y.; Han, Y.; Mukhopadhyay, A.; Yang, L.; Zhu, H. Freestanding Metallic 1T MoS<sub>2</sub> with Dual Ion Diffusion Paths as High Rate Anode for Sodium-Ion Batteries. *Adv. Funct. Mater.* **2017**, *27*, 1702998. [[CrossRef](#)]
43. Kuttly, T.R.N. A controlled copper-coating method for the preparation of ZnS:Mn DC electroluminescent powder phosphors. *Mater. Res. Bull.* **1991**, *26*, 399–406. [[CrossRef](#)]
44. Chen, T.W.; Rajaji, U.; Chen, S.M.; Li, Y.L.; Ramalingam, R.J. Ultrasound-assisted synthesis of alpha-MnS (alabandite) nanoparticles decorated reduced graphene oxide hybrids: Enhanced electrocatalyst for electrochemical detection of Parkinson's disease biomarker. *Ultrason. Sonochem.* **2019**, *56*, 378–385. [[CrossRef](#)]
45. Xin, Y.; Cao, L.; Huang, J.; Liu, J.; Fei, J.; Yao, C. Influence of S/Mn molar ratio on the morphology and optical property of  $\gamma$ -MnS thin films prepared by microwave hydrothermal. *J. Alloys Compd.* **2013**, *549*, 1–5.
46. Rastogi, A.C.; Salkalachen, S.; Bhide, V.G. Electrical conduction and phase transitions in vacuum-deposited Cu<sub>2-x</sub>S films. *Thin Solid Films* **1978**, *52*, 1–10. [[CrossRef](#)]
47. Wang, Y.; Long, Z.; Cheng, Y.; Zhou, M.; Chen, H.; Zhao, K.; Shi, X. Chemical bonding engineering for high-symmetry Cu<sub>2</sub>S-based materials with high thermoelectric performance. *Mater. Today Phys.* **2023**, *32*, 101028. [[CrossRef](#)]
48. Liang, X.; Jin, D.; Dai, F. Phase Transition Engineering of Cu<sub>2</sub>S to Widen the Temperature Window of Improved Thermoelectric Performance. *Adv. Electron. Mater.* **2019**, *5*, 1900486. [[CrossRef](#)]
49. Evans, H.T. Djurleite (Cu<sub>1.94</sub>S) and low chalcocite (Cu<sub>2</sub>S): New crystal structure studies. *Science* **1979**, *203*, 356–358. [[CrossRef](#)]
50. He, Y.; Lu, P.; Shi, X.; Xu, F.; Zhang, T.; Snyder, G.J.; Uher, C.; Chen, L. Ultrahigh Thermoelectric Performance in Mosaic Crystals. *Adv. Mater.* **2015**, *27*, 3639–3644. [[CrossRef](#)]
51. Yao, Y.; Zhang, B.P.; Pei, J.; Sun, Q.; Nie, G.; Zhang, W.Z.; Zhuo, Z.T.; Zhou, W. High Thermoelectric Figure of Merit Achieved in Cu<sub>2</sub>S(1-x)Te(x) Alloys Synthesized by Mechanical Alloying and Spark Plasma Sintering. *ACS Appl. Mater. Interfaces* **2018**, *10*, 32201–32211. [[CrossRef](#)] [[PubMed](#)]
52. Yang, M.; Liu, X.; Zhang, B.; Chen, Y.; Wang, H.; Yu, J.; Wang, G.; Xu, J.; Zhou, X.; Han, G. Phase Tuning for Enhancing the Thermoelectric Performance of Solution-Synthesized Cu<sub>2-x</sub>S. *ACS Appl. Mater. Interfaces* **2021**, *13*, 39541–39549. [[CrossRef](#)]
53. Chen, X.Q.; Fan, S.J.; Han, C.; Wu, T.; Wang, L.J.; Jiang, W.; Dai, W.; Yang, J.P. Multiscale architectures boosting thermoelectric performance of copper sulfide compound. *Rare Met.* **2021**, *40*, 2017–2025. [[CrossRef](#)] [[PubMed](#)]
54. Zhang, R.; Pei, J.; Han, Z.J.; Wu, Y.; Zhao, Z.; Zhang, B.P. Optimal performance of Cu<sub>1.8</sub>S<sub>1-x</sub>Te<sub>x</sub> thermoelectric materials fabricated via high-pressure process at room temperature. *J. Adv. Ceram.* **2020**, *9*, 535–543. [[CrossRef](#)]

**Disclaimer/Publisher's Note:** The statements, opinions and data contained in all publications are solely those of the individual author(s) and contributor(s) and not of MDPI and/or the editor(s). MDPI and/or the editor(s) disclaim responsibility for any injury to people or property resulting from any ideas, methods, instructions or products referred to in the content.